Modeling and Control of a Snake-Like Robot Using the Screw-Drive Mechanism

Hiroaki Fukushima, *Member, IEEE*, Shogo Satomura, Toru Kawai, Motoyasu Tanaka, Tetsushi Kamegawa, and Fumitoshi Matsuno, *Member, IEEE*

***Abstract*—In this paper, we develop a new type of snake-like robot using screw-drive units that are connected by active joints. The screw-drive units enable the robot to generate propulsion on any side of the body in contact with environments. Another feature of this robot is the omnidirectional mobility by combinations of screws' angular velocities. We also derive a kinematic model and apply it to trajectory tracking control. Furthermore, we design a front-unit-following controller, which is suitable for manual operations. In this control system, operators are required to command only one unit in the front; then, commands for the rest of the units are automatically calculated to track the path of the preceding units. Asymptotic convergence of the tracking error of the front-unit-following controller is analyzed based on a Lyapunov approach for the case of constant curvature. The effectiveness of the control method is demonstrated by numerical examples and experiments.**

***Index Terms*—Path tracking, screw-drive mechanism, search and rescue, snake-like robot.**

I. Introduction

MOBILE robots for search and rescue operations in hazardous environments have been actively studied in recent years. One promising type of rescue robots is the so-called snake-like robot, which is typically composed of three or more segments that are connected serially. Because of the long and slender shape, snake-like robots are expected to be effective for searches in narrow spaces and over rubbles in quake-devastated regions, etc. [1], [2]. In addition, snake-like robots for pipe inspection have been reported in the literature [3], [4]. A conventional way of locomotion for snake-like robots is the one by undulations, which imitates real snakes' movements [5]–[15]. However, this type of locomotion needs a width for undulations, which is larger than the width of the robot.

On the other hand, snake-like robots that are driven by crawler mechanisms have been developed [1], [2]. One limitation of typical crawler-type robots arises in vertically narrow spaces, where the upper part of the robots could hit the ceiling. In those cases, the robots could be stuck easily, since the upper and lower parts of the crawlers drive the robot in opposite directions. To overcome this limitation, recent studies have proposed snake-like robots that have crawlers on both upper and lower sides of the body [16], [17].

Locomotion mechanisms that are related to the robot in this paper are found for pipe inspection robots [18]–[20]. While they move by rotating a screw-like device, they are composed of one or two units and have a quite different structure from most snake-like robots. On the other hand, snake-like robots for pipe inspection are also studied in the literature [3], [4]. They form a sinusoidal wave using the whole body and move forward by switching the units pushing the pipe wall. Since these robots are designed specifically for inspection of small diameter pipes, they are not necessarily suitable for other applications such as search and rescue operations.

In this paper, we develop a new type of snake-like robot using the screw-drive mechanism. The original concept is reported in our patent [21]. This robot is composed of screw-drive units, which are connected by active joints serially. Since propulsion is generated by rotating the screws, undulation is not necessary to move. Thus, this robot can go into spaces as narrow as the width of the body. In addition, it is expected that this robot does not get stuck easily even if the upper part of the body hit the ceiling, since the upper part of the screw units drives the body in the same direction as the lower part. Furthermore, unlike most existing snake-like robots, it can move in any direction by a proper combination of screws' angular velocities.

As the first step toward the control system design of the robot potentially having such attractive properties, we derive a kinematic model in the case where the robot does not contact with the environment except for the ground. Because of the switching of the passive wheels in contact with the ground, the motion of the robot is complex even if the ground is flat and horizontal. In order to derive a simple kinematic model for control design, we represent the behavior of the screw unit using a velocity constraint at the center of the unit. While this velocity constraint is quite different from that of the conventional snake-like robots due to the screws, a kinematic model can be derived in

Manuscript received August 11, 2011; accepted December 24, 2011. Date of publication January 31, 2012; date of current version June 1, 2012. This paper was recommended for publication by Associate Editor K. Hosoda and Editor B. J. Nelson upon evaluation of the reviewers' comments. This work was supported in part by the Ministry of Education, Culture, Sports, Science and Technology Grant-in-Aid for Scientific Research (No. 23360105). This paper was presented in part at the IEEE International Conference on Robotics and Automation, Rome, Italy, April 2007 and the IEEE/RSJ International Conference on Intelligent Robots and Systems, Nice, France, September 2008.

H. Fukushima and F. Matsuno are with the Department of Mechanical Engineering and Science, Kyoto University, Kyoto 606-8501, Japan (e-mail: fuku@me.kyoto-u.ac.jp; matsuno@me.kyoto-u.ac.jp).

S. Satomura and M. Tanaka are with Canon, Inc., Tokyo 146-8501, Japan (e-mail: satomura.shogo@canon.co.jp; tanaka.motoyasu@canon.co.jp).

T. Kawai is with Honda R&D Co., Ltd., Saitama 351-0024, Japan (e-mail: toru.kawai@h.rd.honda.co.jp).

T. Kamegawa is with the Graduate School of Natural Science and Technology, Okayama University, Okayama 700-8530, Japan (e-mail: kamegawa@sys.okayama-u.ac.jp).

Color versions of one or more of the figures in this paper are available online at http://ieeexplore.ieee.org.

Digital Object Identifier 10.1109/TRO.2012.2183050

the same way as the conventional snake-like robots moving by undulations [6]–[8], once the velocity constraint is obtained. To examine the validity of the model, both feedback and feedforward controllers, which are designed using the model, are applied to the robot.

Even if the feedback controller to steer the robot to the target state is designed, a hard problem remained is how to determine the target state of the robot. For searches in narrow spaces, human operators typically need to determine the target state. However, it is hard for operators to give commands for all joints as well as the head position and orientation, such that the shape of the robot is fit to the narrow space.

In [1], a front-unit-following control system has been implemented to reduce difficulties in manual operations of a crawler-type snake robot. The operators are required to command only one unit in the head of the robot; then, commands for the rest of the units are automatically calculated to track the path of the preceding units. While the effectiveness of the control law has been demonstrated by experiments, theoretical analysis on the tracking performance is still a challenging issue. In addition, it is not straightforward to apply the method in [1] to the robot using the screw-drive mechanism, due to the difference of the locomotion mechanism. Related to the front-unit-following control of snake robots, path-tracking control methods for articulated vehicles have been studied in the literature (see, e.g., [22]–[24]). However, these methods assume that the target path for each unit is given, since they are based on feedback of tracking error from the target path. Thus, in order to apply these methods to front-unit-following control, the target path needs to be estimated based on the memory of the past commands to the front unit, which is difficult in many cases due to the computational burden.

In this paper, we design a front-unit-following control law using only the current velocity commands to the front unit. More precisely, the velocity of each unit is determined by assuming that the transition rate of curvature of the target path is sufficiently small in a local section between two consecutive joints of the robot, and that each unit is currently on the target path. Since this implies that a rapid change of curvature of the target path causes a large tracking error, it is important to find conditions where off-tracking can be recovered by the proposed control law. Thus, we also analyze the asymptotic convergence of the tracking error based on a Lyapunov approach for the case where the curvature of the target path is constant. The effectiveness of the control method is demonstrated by simulations and experiments including the cases where the curvature of the target path is not constant.

II. Snake-like Robot with Screw-Drive Mechanism

A. Outline of the Robot System

Fig. 1 shows a prototype of the snake-like robot using the screw-drive mechanism. The robot is composed of two types of screw-drive units, i.e., "left" and "right" screw units. In Fig. 1, right and left units are connected alternatively from the head to the tail. The screw-drive units are connected by 2-degree-of-freedom (DOF) active joints. Moreover, a caster with ball bearings is set up at the head of the robot to prevent the body inside the unit from rotating instead of the screws, when the shape of the robot is straight. As shown in Fig. 2, each screw-drive unit has a dc motor (A-max22, Maxon) inside to rotate the screw which is the outer part of the unit.

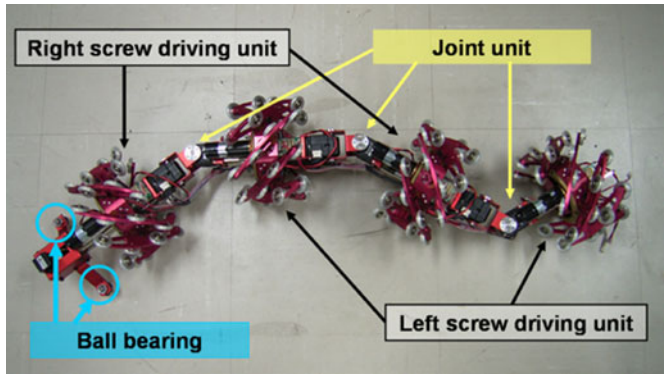

Fig. 1. Snake-like robot using the screw-drive mechanism.

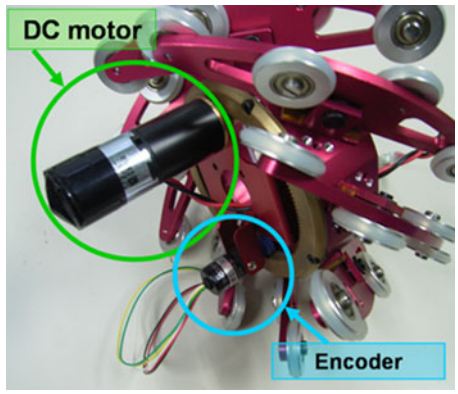

Fig. 2. Screw-drive unit.

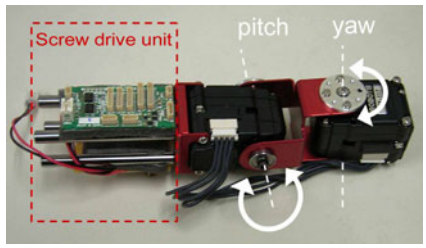

Fig. 3. Joint unit.

Fig. 3 shows a joint unit, which has two motors (Dynamixel DX-117, Robotis) for pitch and yaw angles. The range of movement of each motor is constrained to $\pm\frac{\pi}{2}$ rad. Feedback controllers for angular position and velocity are included inside the motors. All the motors for joint units are connected in a daisy chain and communicate each other using RS485. Note that the pitch angle of each joint is controlled to 0 rad, since we only consider the cases where the ground is flat in this paper.

Fig. 4 illustrates the structure of the control system, which is divided into two main parts, the screw-drive unit part and the joint unit part. The screw-drive unit part communicates with a personal computer (PC) by using RS232C, and the joint unit part

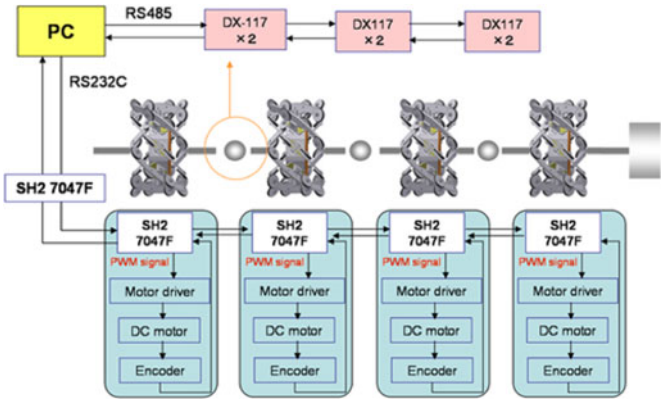

Fig. 4. Schematic of the control system.

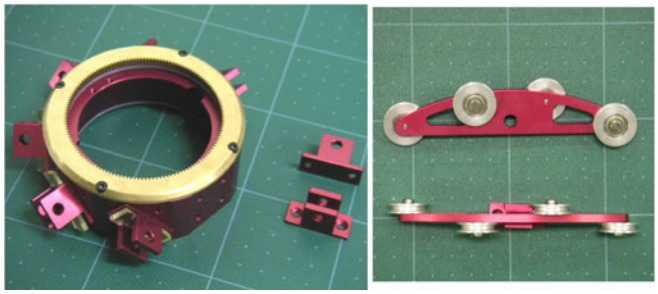

Fig. 5. Components of a screw.

communicates with the PC by using RS485. For velocity control of a screw, a target value of the angular velocity is first sent from the PC to the microcomputer (TITech SH2 Tiny Controller, HiBot). Then, a pulsewidth modulation (PWM) signal is given from the microcomputer to the motor driver (1Axis DC Power Module, HiBot) to drive the dc motor. Count values of the encoders (MEH-9-360PC, Microtech Laboratory) are obtained by the microcomputers as rotation angle data of the screw part. One microcomputer is used for each screw-drive unit, and another one attached to the tail of the robot is used for a relay between the units and the PC. The microcomputers communicate with each other by using the controller area network (CAN).

B. Screw-Drive Unit

A screw-drive unit (see Fig. 2) is composed of the screw part (see Fig. 6) which actually rotates, and the inner body which is equipped with a dc motor to drive the screw part. The screw part is composed of a ring-shaped part as shown in Fig. 5 (left), which is substantially a hollow regular octagonal prism having a ring gear in front. A blade as shown in Fig. 5 (right) is attached at the center of each side of the octagonal prism. Four passive wheels are attached to each blade. Note that each passive wheel has a rubber ring around the rim to provide more friction, as shown in Fig. 2.

As shown in Fig. 6, we define the local coordinate system $O-XYZ$ which is attached to a screw-drive unit. The X-axis is set along the rotation axis of the screw, and the positive direction of the X-axis points toward the back of the screw. The Y- and Z-axes are set so as to pass through the centers of the

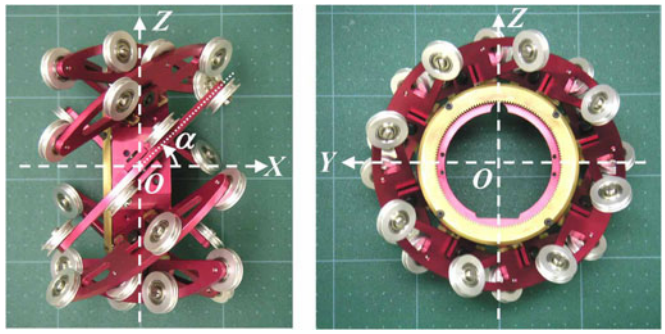

Fig. 6. Side and front views of a screw.

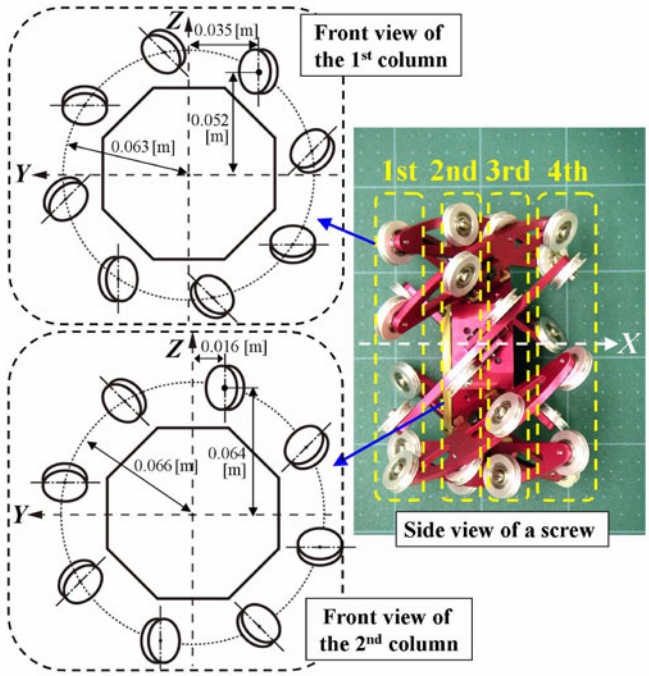

Fig. 7. Alignment of passive wheels (left screw-drive unit).

sides of the octagonal prism. We also define α ($-\frac{\pi}{2} < \alpha \leq \frac{\pi}{2}$) as the angle of the blade from the X-axis when viewed from the outside of the screw, as shown in Fig. 6 (left). If a unit has positive (negative) α, we refer to it as a left (right) screw-drive unit. Further, α_i is defined as the angle α of the ith screw unit.

As shown in the side view of the screw in Fig. 7 (right), a screw unit has four columns of passive wheels. In each column, the passive wheels are aligned on a circle in a plane perpendicular to the rotation axis of the screw. Two figures in Fig. 7 (left) show the front views of the wheels in the first and second columns. The center of each passive wheel is located on a circle shown in the dotted line. Each wheel is inclined at α about the axis shown in a dash–dotted line, which passes through the center of the passive wheel and is perpendicular to a side of the octagonal prism. Note that the positions of the wheels in the third (fourth) column are symmetric to the ones in the second (first) column with respect to the Z-axis. As a result, the wheels in the first (second) column are located at similar positions on the Y–Z plane to the wheels in the third (fourth) column. It is also seen from Fig. 7 that the

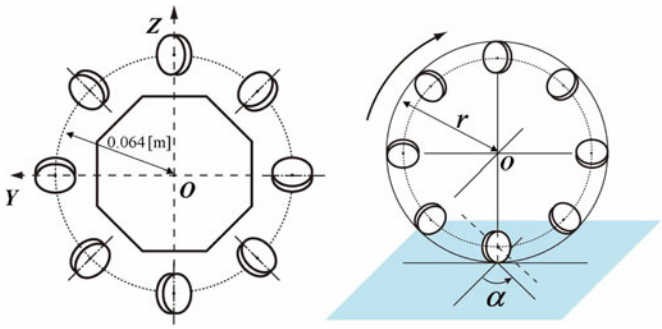

Fig. 8. Simplified screw model (left: front view, right: relation to the ground).

distance from the rotation axis of the screw to the passive wheels in the second and third columns is longer than the distance to the wheels in the first and fourth columns. This implies that if the ground is flat and horizontal, and if the pitch angles of the joints are controlled to 0, a wheel in the second column and one in the third column alternately contact with the ground. Further, at the moments when the wheel contacting with the ground is switched, two wheels contact with the ground at the same time. However, it is difficult to construct a model taking into account such switching properties of the passive wheel in contact with the ground. Thus, in order to describe the average behavior of the screw unit, we assume that the passive wheels as shown in Fig. 8 (left) exist at $X = 0$ in the middle of the second and the third columns, and that only one of these wheels contacts with the ground without side slip. In addition, we assume that a perpendicular line from O to the ground passes through the contact point with the ground, as shown in Fig. 8 (right). In this case, the rotation axis of the passive wheel on the ground is parallel to the ground; therefore, its projection to the ground is inclined at α from the rotation axis of the screw.

Because of the assumptions mentioned earlier on the relationship between the passive wheels and the ground, our model that is used in this paper has a limitation in describing the real robot, even in the case where the ground is flat and horizontal. Further, since the ground is not completely flat in reality, two or more of the passive wheels of one unit can contact with the ground. In such situations, it is difficult for the units to change the orientation without side slip of passive wheels. Despite these complex properties of the robot, we start with a simpler model for control design based on the assumptions mentioned earlier, since a complex model describing the robot more exactly is not easy to obtain and is not necessarily useful for control design.

III. Kinematic Model

In this section, we derive a kinematic model of the robot that is composed of four screw-drive units described in Section II.

As shown in Fig. 9, let o be the origin of the absolute coordinate system, P be the point to be controlled in the head of the robot, and o-xy be the absolute coordinate system. In addition, let $[x_p\ y_p\ \psi_p]^T$ be the absolute coordinate of P and the orientation of unit 1. The positions of the center of the screw unit i and the joint i are defined as $[x_i\ y_i]^T$ and $[x_{ji}\ y_{ji}]^T$, respectively. Furthermore, let L_1 be the length from the front tip of each link

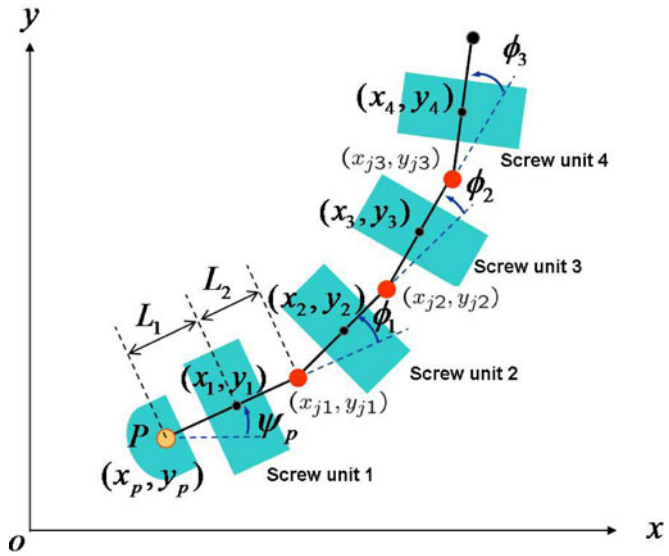

Fig. 9. Definition of coordinate variables.

to the center of the screw-drive unit on the link, and L_2 be the length from the center of the screw unit to the rear end of the link. The joint angle ϕ_i is defined as the orientation of the unit i with respect to the unit $i-1$, and $\psi_i = \psi_p + \sum_{k=1}^{i-1} \phi_k (i = 2, 3, 4)$ denotes the orientation of the unit i with respect to the absolute coordinate system. Additionally, let $\dot{\theta}_i (i = 1, 2, 3, 4)$ be the angular velocity of the screw-drive unit i.

The position of the center of the screw unit i is described from a geometrical relation as follows:

$$x_i = x_p + L_1 \cos\psi_p + \sum_{j=1}^{i-1} (L_2 \cos\psi_j + L_1 \cos\psi_{j+1})$$

$$y_i = y_p + L_1 \sin\psi_p + \sum_{j=1}^{i-1} (L_2 \sin\psi_j + L_1 \sin\psi_{j+1}) \quad (1)$$

where $\psi_1 := \psi_p$. Since it is assumed that the passive wheels do not slip sideways, we need to take into account the velocity constraint condition. The velocity constraint condition here is more complicated than conventional snake-like robots [6]–[8] because of the screw units. As shown in Fig. 10, if the screw-drive unit i rotates at angular velocity $\dot{\theta}_i$, the velocity $r\dot{\theta}_i$ is generated for the passive wheel, where r denotes the radius of the screw-drive unit (distance from the rotation axis of the unit to the ground) as shown in Fig. 8. At the same time, if the center of the screw unit moves with the velocity $(\dot{x}_i,\ \dot{y}_i)$, the same velocity is generated for the passive wheel. Fig. 11 shows the top view of the passive wheel on the ground and the velocities that are generated for the passive wheel. The component of the velocity $r\dot{\theta}_i$ in the direction of the axle of the passive wheel is $r\dot{\theta}_i \sin\alpha_i$. The x- and y-components $(\dot{x}_i, \dot{y}_i)$ of the translational velocity of the unit i, respectively, generate $\dot{x}_i \cos(\alpha_i + \psi_i)$ and $\dot{y}_i \sin(\alpha_i + \psi_i)$ in the direction of the axle of the passive wheel. Therefore, the velocity constraint is described as follows:

$$\dot{x}_i \cos(\alpha_i + \psi_i) + \dot{y}_i \sin(\alpha_i + \psi_i) + r\dot{\theta}_i \sin\alpha_i = 0. \quad (2)$$

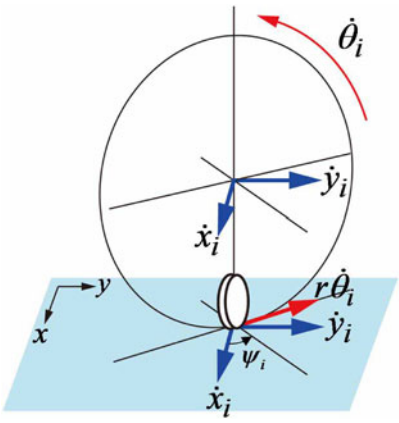

Fig. 10. Velocities generated for a passive wheel.

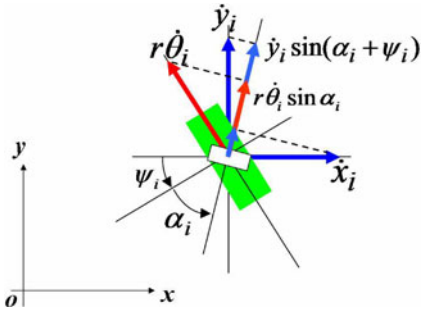

Fig. 11. Velocity constraint for a passive wheel (top view).

By substituting the derivatives of (1) into (2), the following kinematic model is obtained:

$$A\dot{\xi} = Bu \tag{3}$$

where $\xi = [x_p \ y_p \ \psi_p \ \phi_1 \ \phi_2 \ \phi_3]^T$ is the state vector to be controlled, and $u = [\dot{\theta}_1 \ \dot{\theta}_2 \ \dot{\theta}_3 \ \dot{\theta}_4 \ \dot{\phi}_1 \ \dot{\phi}_2 \ \dot{\phi}_3]^T$ is the control input vector. The system matrices A and B are defined as follows:

$$A := \left[\begin{array}{c|c} A_{11} & A_{12} \\ \hline \mathbf{0} & E_3 \end{array}\right], \quad B := \text{block diag}(B_1, E_3)$$

$$A_{11} := \begin{bmatrix} a_{11} & a_{12} & a_{13} \\ a_{21} & a_{22} & a_{23} \\ a_{31} & a_{32} & a_{33} \\ a_{41} & a_{42} & a_{43} \end{bmatrix}, \quad A_{12} := \begin{bmatrix} 0 & 0 & 0 \\ a_{24} & 0 & 0 \\ a_{34} & a_{35} & 0 \\ a_{44} & a_{45} & a_{46} \end{bmatrix}$$

$$B_1 := -r \ \text{diag}(\sin\alpha_1, \sin\alpha_2, \sin\alpha_3, \sin\alpha_4)$$

$$a_{i1} := \cos(\alpha_i + \psi_i), \quad a_{i2} := \sin(\alpha_i + \psi_i)$$

$$a_{13} := L_1 \sin\alpha_1, \quad a_{23} := L\sin(\alpha_2 + \phi_1) + L_1 \sin\alpha_2$$

$$a_{24} := L_1 \sin\alpha_2, \quad a_{33} := L\sin(\alpha_3 + \phi_1 + \phi_2) + a_{34}$$

$$a_{34} := L\sin(\alpha_3 + \phi_2) + L_1 \sin\alpha_3, \quad a_{35} := L_1 \sin\alpha_3$$

$$a_{43} := L\sin(\alpha_4 + \phi_1 + \phi_2 + \phi_3) + a_{44}$$

$$a_{44} := L\sin(\alpha_4 + \phi_2 + \phi_3) + a_{45}$$

$$a_{45} := L\sin(\alpha_4 + \phi_3) + L_1 \sin\alpha_4, \quad a_{46} := L_1 \sin\alpha_4 \tag{4}$$

where $L := L_1 + L_2$, and E_k denotes the identity matrix of size k. In our experimental system, the values of parameters are $L_1 = 0.103$ m, $L_2 = 0.123$ m, $r = 0.075$ m, $\alpha_i = -\frac{\pi}{4}$ rad$(i = 1, 3)$, and $\alpha_i = \frac{\pi}{4}$ rad$(i = 2, 4)$.

Remark 1: If the upper part of the screw unit contacts with the environment in the same way as the lower part, we have another velocity constraint

$$\dot{x}_i \cos(-\alpha_i + \psi_i) + \dot{y}_i \sin(-\alpha_i + \psi_i) - r\dot{\theta}_i \sin(-\alpha_i) = 0$$

for the passive wheel in contact with the ceiling. From this constraint together with (2), we obtain

$$\dot{x}_i \cos\psi_i + \dot{y}_i \sin\psi_i + r\dot{\theta}_i \tan\alpha_i = 0$$
$$\dot{x}_i \sin\psi_i - \dot{y}_i \cos\psi_i = 0.$$

Note that the second equation implies that the component, which is perpendicular to the link, of the velocity $(\dot{x}_i, \dot{y}_i)$ at the center of the unit is 0. This implies that the upper and lower parts cooperatively drive the unit into the direction along the rotation axis, in contrast with most crawler units whose upper and lower parts generate the velocity in the opposite directions at the center of the unit.

IV. Trajectory Control

For the system in (3), a control law for trajectory tracking is designed as follows:

$$u = B^{-1}A(\dot{\xi}_d - Ke) \tag{5}$$

where $e = \xi - \xi_d$, ξ_d is a given target trajectory, and K is a given feedback gain matrix. We notice that B is invertible if $\alpha_i \neq 0$ $(i = 1, 2, 3, 4)$.

By substituting (5) into (3), the closed-loop system is given as follows:

$$A(\dot{e} + Ke) = 0. \tag{6}$$

If the matrix A is not of full column rank, then it holds $\dot{e} + Ke = 0$. Therefore, $\xi \to \xi_d$ $(t \to \infty)$ is guaranteed if K is positive definite. On the other hand, if A is not of full column rank, the convergence of ξ is not guaranteed, since $\dot{e} + Ke = 0$ does not necessarily hold. Appendix A describes a necessary condition of the joint angles (ϕ_1, ϕ_2), for which A does not have full column rank. As mentioned at the end of Appendix A, the necessary condition is satisfied in the case where the robot has a zig–zag shape with $\phi_1 - \phi_2 > 2.35$ rad and $\phi_2 < -1.35$ rad, or in the case where $\phi_i \simeq \frac{\pi}{2}$ or $-\frac{\pi}{2}$ $(i = 1, 2)$. In our target applications such as searches in narrow spaces, the target angles are typically chosen away from these values, since these values require wider space for the robot to pass through.

A. Numerical Examples

We show an example of our simulation results where the target path of the head position P is given as an arc of radius $R_p = 0.8$ m, as shown in Fig. 12. Target joint angles are chosen such that each joint position tracks the circular path if P tracks

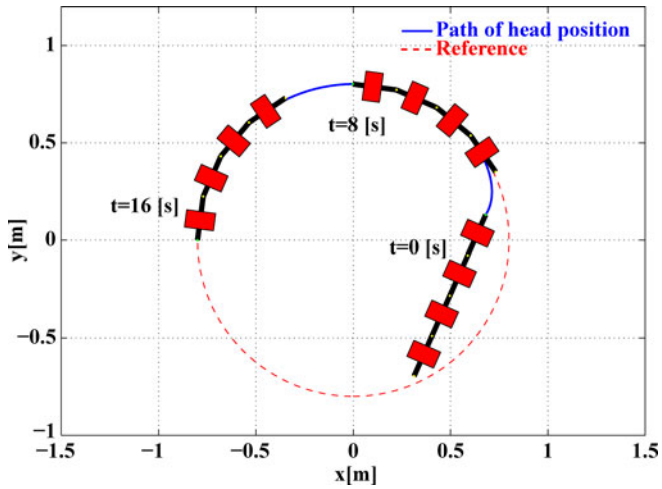

Fig. 12. x–y plot of the head position in simulation (feedback).

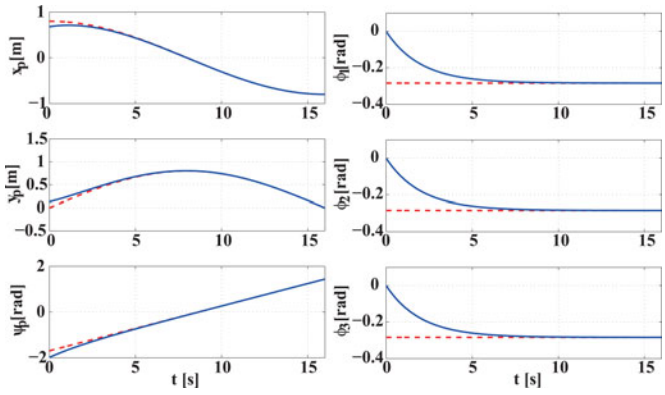

Fig. 13. Time responses of the state variables in simulation (feedback).

it. More precisely, the target trajectory ξ_d is chosen as

$$\xi_d = [R_p \cos\frac{\pi}{16}t, R_p \sin\frac{\pi}{16}t, \frac{\pi}{16}t - \frac{\pi}{2} - \frac{\phi_d}{2}, \phi_d, \phi_d, \phi_d]^T$$

$$\phi_d := -2\sin^{-1}\frac{L}{2R_p} = -0.283.$$

The feedback gain in (5) and the initial state are $K = 0.5E_6$ and $\xi(0) = [1.48, 0.13, -1.99, 0, 0, 0]^T$, respectively.

Fig. 12 shows an x–y plot of the trajectory of the head position P, and Fig. 13 indicates the time responses of the state variables. The solid and dashed lines in the figures show the state responses and the target trajectories, respectively. From these figures, it can be seen that the state variables converge to the desired trajectory, and the robot moves along the target path.

B. Experiments

We first compare the responses of the head position P by feedforward and feedback controls for fixed joint angles. The position and orientation of the head $[x_p, y_p, \psi_p]^T$ are measured by a vision sensor system (QuickMag IV, OKK). The target trajectory ξ_d is chosen as

$$\xi_d = \left[R_p \cos\frac{\pi}{12}t, R_p \sin\frac{\pi}{12}t, \frac{\pi}{12}t - \frac{\pi}{2}, 0, 0, 0\right]^T, R_p = 0.7.$$

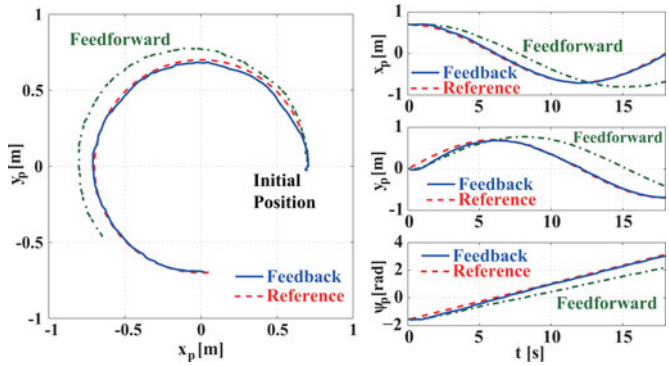

Fig. 14. Experimental results for fixed joint angles (feedback and feedforward).

Since both the initial and target angles of joints are 0 rad, joint angles are fixed to $\phi_1 = \phi_2 = \phi_3 = 0$ rad. Fig. 14 shows an x–y plot of the head position P (left column) and the time responses of (x_p, y_p, ψ_p) (right column). The solid line shows the response by feedback control for $K = 0.5E_6$, whereas dash–dotted line shows the response by feedforward control, i.e., $K = 0$. In Fig. 14, the response by feedforward control is significantly slower than the target trajectory, which causes large tracking error of P. This shows that our model is not correct enough to describe the real system. If the model is correct, we have $\dot{e} = 0$ from (6) for A of full column rank. Since the initial tracking error is 0 in this example, ξ should always be equal to ξ^d even if $K = 0$. A possible reason for this modeling error is that the assumptions for the passive wheels on the ground do not hold. On the other hand, all the variables are well controlled to the target trajectories by applying the feedback control. Thus, the uncertainty of our model can be considered to be within the allowable level for control design. Construction of more complex models that describe the real robot more exactly and control design based on such complex models are possible future works.

Next, we show a similar case to the numerical example in Section IV-A where the joint angles are changed. The same values of ξ_d, $\xi(0)$ and K are chosen as in Section IV-A. Fig. 15 shows an x–y plot of the head position P, and Fig. 16 indicates the time responses of the state variables. These figures show that the head position P tracks the target trajectory with similar performance to the fixed joint case in Fig. 14. However, the steady-state error which is not seen in the simulation result in Fig. 13 is caused for each state. Possible reasons, except for violation of the assumptions on the passive wheels as mentioned earlier, are slight rotation of the body inside the screw units and the load due to the communications cables.

V. Front-Unit-Following Control

In Section IV, a feedback control system to steer the head position and orientation as well as joint angles to given target values has been designed based on a kinematic model. However, in typical practical situations where a human operator manipulates the robot watching images from a camera attached to the head, it is hard for operators to give commands for all joints as

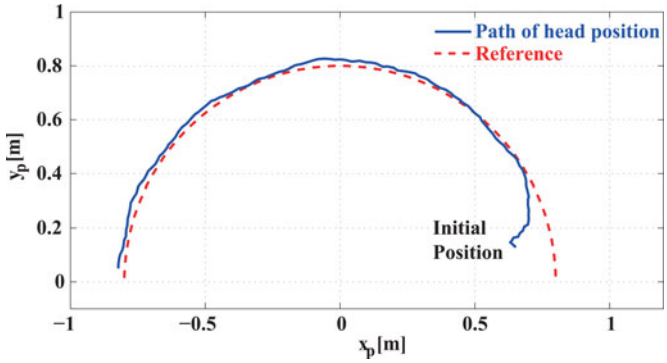

Fig. 15. x–y plot of the head position in experiment (feedback).

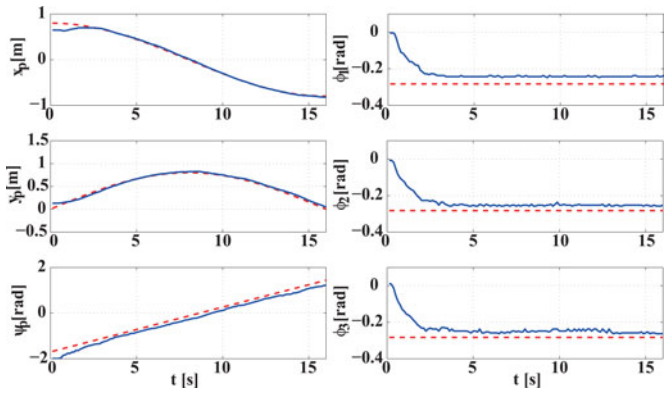

Fig. 16. Time responses of the state variables in experiment (feedback).

well as the head position and orientation, such that the shape of the robot is adapted to narrow spaces.

In this section, we propose a front-unit-following control method for the snake-like robot using the screw-drive mechanism, and show numerical examples and experimental results to evaluate the effectiveness of the proposed method.

A. Control Objective

The main goal of this section is to fit the robot shape to the path of the front unit for the given $(\dot{x}_p, \dot{y}_p, \dot{\psi}_p)$, by controlling the joint angles. In order to fit the robot shape to the path of the front unit, it is desired that each joint is controlled to the path of the head position P. However, since $\dot{\psi}_p$ is not a manipulated variable but given in advance, it is difficult to control joint 1 to the path γ' of P, as shown in Fig. 17. Thus, we aim to determine $(\dot{\phi}_1, \dot{\phi}_2, \dot{\phi}_3)$ such that each joint follows the path γ of joint 1. In addition, we determine $(\dot{\theta}_1, \dot{\theta}_2, \dot{\theta}_3, \dot{\theta}_4)$ which realizes the given $(\dot{x}_p, \dot{y}_p, \dot{\psi}_p)$.

In particular, we focus on two special cases as follows.

Case (i): A typical situation in manual operation, where $(\dot{x}_p, \dot{y}_p, \dot{\psi}_p)$ are given as

$$\dot{x}_p = -v_1 \cos\psi_p, \quad \dot{y}_p = -v_1 \sin\psi_p, \quad \dot{\psi}_p = \omega_1 \tag{7}$$

using the velocity commands (v_1, ω_1) given by a human operator. A control method without using measurement data of (x_p, y_p, ψ_p) is typically required in this case, since a human operator often determines (v_1, ω_1) watching images from a camera

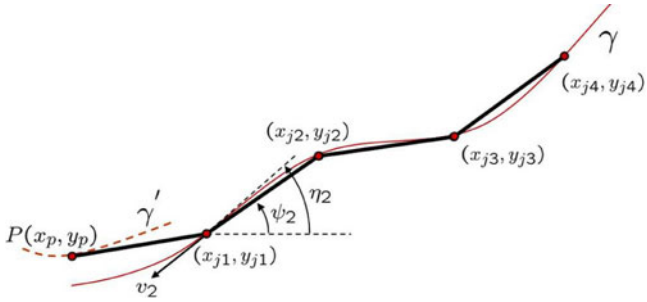

Fig. 17. Target path γ and joint positions.

attached to the robot, and no sensor for measuring (x_p, y_p, ψ_p) is available.

Case (ii): If (x_p, y_p, ψ_p) are measured, the following feedback law can be applied:

$$\dot{\xi}_1 = \dot{\xi}_{d1} - K_1(\xi_1 - \xi_{d1}), \quad \xi_1 := [x_p, y_p, \psi_p]^T \tag{8}$$

where K_1 is a feedback gain, and ξ_{d1} is a given target trajectory of ξ_1. This is a similar situation to Section IV, where a target trajectory of (x_p, y_p, ψ_p) is given in advance.

B. Decision of Control Input

Assume that joint positions (x_{j2}, y_{j2}), (x_{j3}, y_{j3}), (x_{j4}, y_{j4}) are initially on the path γ of the first joint (x_{j1}, y_{j1}) at $t = 0$, as shown in Fig. 17. Then, path tracking is accomplished at each time $t \geq 0$, if the velocity of each joint is always generated in the tangential direction of γ.

From (7) and a geometric relationship

$$\begin{aligned} x_{j1} &= x_p + L\cos\psi_p \\ y_{j1} &= y_p + L\sin\psi_p \end{aligned} \tag{9}$$

the target velocity of joint 1 is described as

$$\begin{aligned} \dot{x}_{j1} &= \dot{x}_p - L\dot{\psi}_p \sin\psi_p \\ \dot{y}_{j1} &= \dot{y}_p + L\dot{\psi}_p \cos\psi_p. \end{aligned} \tag{10}$$

Let η_{i+1} denote the orientation of the tangent vector of γ at the position (x_{ji}, y_{ji}) of the joint i $(i = 2, 3)$. Then, the target translational velocity v_{i+1} of the joint i and the target angular velocity $\dot{\psi}_i$ of the unit i need to satisfy

$$\begin{aligned} \dot{x}_{ji} &= \dot{x}_{j(i-1)} - L\dot{\psi}_i \sin\psi_i = -v_{i+1}\cos\eta_{i+1} \\ \dot{y}_{ji} &= \dot{y}_{j(i-1)} + L\dot{\psi}_i \cos\psi_i = -v_{i+1}\sin\eta_{i+1}. \end{aligned} \tag{11}$$

By solving (11), $\dot{\psi}_i$ and v_{i+1} for path tracking are derived as

$$\dot{\psi}_i = \frac{\dot{x}_{j(i-1)}\sin\eta_{i+1} - \dot{y}_{j(i-1)}\cos\eta_{i+1}}{L\cos(\psi_i - \eta_{i+1})} \tag{12}$$

$$v_{i+1} = -\frac{\dot{x}_{j(i-1)}\cos\psi_i + \dot{y}_{j(i-1)}\sin\psi_i}{\cos(\psi_i - \eta_{i+1})}. \tag{13}$$

Note that η_{i+1} is equivalent to a past value of η_i, since the coordinate (x_{ji}, y_{ji}) of the joint i is a position where the joint $i-1$ passed in the past. Thus, in order to obtain η_{i+1}, the past data, e.g., $(\dot{x}_{j1}, \dot{y}_{j1})$ in (10), need to be stored.

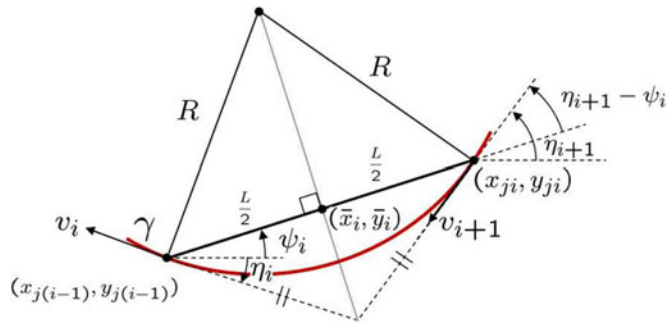

Fig. 18. Target path between two joints.

In this paper, we adopt a simpler algorithm without using past data, by assuming that the transition rate of curvature of the target path γ is sufficiently small between two consecutive joints. In such cases, it is satisfied that

$$\eta_{i+1} - \psi_i = \psi_i - \eta_i \tag{14}$$

since the directions of v_{i+1} and v_i are symmetric with respect to the link i, as shown in Fig. 18. In addition, since (11) implies that

$$\begin{aligned} v_{i+1}\cos(\eta_{i+1} - \psi_i) &= -\dot{x}_{ji}\cos\psi_i - \dot{y}_{ji}\sin\psi_i \\ &= -\dot{x}_{j(i-1)}\cos\psi_i - \dot{y}_{j(i-1)}\sin\psi_i = v_i\cos(\psi_i - \eta_i) \end{aligned} \tag{15}$$

we have $v_{i+1} = v_i$ from (14). Therefore, at the middle point $(\bar{x}_i, \bar{y}_i)$ of each link, the translational velocity $\bar{v}_i$ is generated along the link as follows:

$$\begin{aligned} \dot{\bar{x}}_{ji} &= \dot{x}_{j(i-1)} - \frac{L}{2}\dot{\psi}_i\sin\psi_i = -\bar{v}_i\cos\psi_i \\ \dot{\bar{y}}_{ji} &= \dot{y}_{j(i-1)} + \frac{L}{2}\dot{\psi}_i\cos\psi_i = -\bar{v}_i\sin\psi_i. \end{aligned} \tag{16}$$

By solving (16), we have

$$\begin{aligned} \dot{\psi}_i &= \frac{2}{L}\{\dot{x}_{j(i-1)}\sin\psi_i - \dot{y}_{j(i-1)}\cos\psi_i\} \\ \bar{v}_i &= -\dot{x}_{j(i-1)}\cos\psi_i - \dot{y}_{j(i-1)}\sin\psi_i. \end{aligned} \tag{17}$$

Since $\dot{\phi}_i = \dot{\psi}_{i+1} - \dot{\psi}_i$, input variables $(\dot{\phi}_1, \dot{\phi}_2, \dot{\phi}_3)$ are recursively obtained for the given $(\dot{x}_p, \dot{y}_p, \dot{\psi}_p)$. Once $(\dot{\phi}_1, \dot{\phi}_2, \dot{\phi}_3)$ are determined, the screws' angular velocities $(\dot{\theta}_1, \ldots, \dot{\theta}_4)$ in u can be obtained from the first four rows in (3) as follows:

$$\dot{\theta} = B_1^{-1}A_1\dot{\xi} \tag{18}$$

where $\theta := [\theta_1, \theta_2, \theta_3, \theta_4]^T$, and $A_1 := [A_{11}, A_{12}]$.

In Case (i), it holds from (7), (10), and (17) that

$$\begin{aligned} \bar{v}_2 &= v_1\cos\phi_1 - L\omega_1\sin\phi_1 \\ \dot{\psi}_2 &= -\frac{2}{L}(v_1\sin\phi_1 + L\omega_1\cos\phi_1). \end{aligned} \tag{19}$$

In the same way, velocity commands for the rest of units are recursively determined as

$$\begin{aligned} \bar{v}_i &= \bar{v}_{i-1}\cos\phi_{i-1} - \frac{L}{2}\dot{\psi}_{i-1}\sin\phi_{i-1} \\ \dot{\psi}_i &= -\frac{2}{L}\bar{v}_{i-1}\sin\phi_{i-1} - \dot{\psi}_{i-1}\cos\phi_{i-1} \end{aligned} \tag{20}$$

for $i = 3, 4$. Since $\dot{\psi}_2 = \dot{\psi}_p + \dot{\phi}_1$, the target angular velocity of joint 1, which achieves $\dot{\psi}_2$ in (19), is written as

$$\dot{\phi}_1 = -\frac{2}{L}v_1\sin\phi_1 - \omega_1(2\cos\phi_1 + 1). \tag{21}$$

In addition, from $\dot{\psi}_3 = \dot{\psi}_p + \dot{\phi}_1 + \dot{\phi}_2$, we have

$$\begin{aligned} \dot{\phi}_2 &= -\frac{2}{L}\bar{v}_2\sin\phi_2 - (\omega_1 + \dot{\phi}_1)(\cos\phi_2 + 1) \\ \bar{v}_3 &= \bar{v}_2\cos\phi_2 - \frac{L}{2}(\omega_1 + \dot{\phi}_1)\sin\phi_2 \end{aligned} \tag{22}$$

using (20). In the same way, $\dot{\phi}_3$ is obtained as

$$\dot{\phi}_3 = -\frac{2}{L}\bar{v}_3\sin\phi_3 - (\omega_1 + \dot{\phi}_1 + \dot{\phi}_2)(\cos\phi_3 + 1) \tag{23}$$

using (20) and $\dot{\psi}_4 = \dot{\psi}_p + \dot{\phi}_1 + \dot{\phi}_2 + \dot{\phi}_3$. From (21)–(23), it can be seen that $(\dot{\phi}_1, \dot{\phi}_2, \dot{\phi}_3)$ can be determined without measurement of $(x_p,\ y_p,\ \psi_p)$. In addition, although A_1 and $\dot{\xi}$ depend on ψ_p, it is canceled in (18), since it holds from (4) and (7) that

$$a_{i1}\dot{x}_p + a_{i2}\dot{y}_p = v_1\cos(\alpha_i + \psi_i - \psi_p), \quad i = 1, 2, 3, 4. \tag{24}$$

Thus, the measurement of $(x_p,\ y_p,\ \psi_p)$ is not necessary to determine $\dot{\theta}$ in the case where $(\dot{x}_p, \dot{y}_p, \dot{\psi}_p)$ are given as in (7).

In Case (ii), the closed-loop system for ξ_1 is obtained from (8) and (18) as

$$A_{11}(\dot{e}_1 + K_1e_1) = 0, \quad e_1 := \xi_1 - \xi_{d1}. \tag{25}$$

Thus, if A_{11} is of full column rank, ξ_1 converges to ξ_{d1} as t increases.

C. Convergence for Constant Curvature

The target velocities in Section V-B are derived under assumptions that joint positions are initially on the target path γ, and that the transition rate of curvature of γ is sufficiently small between two consecutive joints. This implies that a rapid change of curvature causes a large path-tracking error. Therefore, it is important to find conditions where off-tracking can be recovered by the proposed control law.

In this section, we show that even if joint positions are initially off the target path γ, they converge to γ in the case where the curvature of γ is constant. More precisely, we consider the case where (v_1, ω_1) is constant in (7). We assume that the robot moves forward, i.e., $v_1 > 0$. The extension of the method to other cases is a subject of future research. In addition, we note that only the case of $\omega_1 < 0$ is described, since the case of $\omega_1 > 0$ is similar. The case of $\omega_1 = 0$, where the path is a straight line, is also omitted, since it is easier to prove.

By integrating (7), the head position P is obtained as

$$x_p = C_x + R_p\sin\psi_p, \quad y_p = C_y - R_p\cos\psi_p \tag{26}$$

where $R_p := -\frac{v_1}{\omega_1} > 0$,

$$C_x := x_0 - R_p\sin\psi_0, \quad C_y := y_0 + R_p\cos\psi_0. \tag{27}$$

In (27), (x_0, y_0, ψ_0) denotes the initial value of (x_p, y_p, ψ_p). Thus, the position of joint 1 is obtained from (9) as

$$\begin{aligned} x_{j1} &= C_x + R_{j1}\sin(\psi_p + \alpha_{j1}) \\ y_{j1} &= C_y - R_{j1}\cos(\psi_p + \alpha_{j1}) \end{aligned} \tag{28}$$

where $R_{j1} = \sqrt{R_p^2 + L^2}$, and α_{j1} is a value that satisfies

$$\cos\alpha_{j1} = \frac{R_p}{R_{j1}}, \quad \sin\alpha_{j1} = \frac{L}{R_{j1}}. \tag{29}$$

Thus, from $L > 0, R_p > 0$, we assume that $0 < \alpha_{j1} < \frac{\pi}{2}$ without loss of generality. It is seen from (28) that joint 1 moves along a circle of radius R_{j1} and center (C_x, C_y). In addition, it holds from (21) that

$$\dot{\phi}_1 = \frac{2R_{j1}\omega_1}{L}\sin(\phi_1 - \alpha_{j1}) - \omega_1. \tag{30}$$

Now, define $V_1 := \frac{1}{2}\Phi_1^2$ for $\Phi_1 := \dot{\phi}_1$, which satisfies $V_1 > 0$ for $\Phi_1 \neq 0$. Then, it holds

$$\dot{V}_1 = \Phi_1\dot{\Phi}_1 = \Phi_1^2\frac{2R_{j1}\omega_1}{L}\cos(\phi_1 - \alpha_{j1}). \tag{31}$$

Since $-\frac{\pi}{2} \le \phi_1 \le \frac{\pi}{2}$ due to the movable range of joints, we consider two cases where $-\frac{\pi}{2} \le \phi_1 \le 0$ and $0 \le \phi_1 \le \frac{\pi}{2}$. In the case of $-\frac{\pi}{2} \le \phi_1 \le 0$, we have $-\pi < \phi_1 - \alpha_{j1} < 0$ since $0 < \alpha_{j1} < \frac{\pi}{2}$. This implies that $\sin(\phi_1 - \alpha_{j1}) < 0$. Thus, the first term on the right-hand side of (30) is positive, since $\omega_1 < 0$. Therefore, in the case of $-\frac{\pi}{2} \le \phi_1 \le 0$, it always holds from (30) that $\dot{\phi}_1 > -\omega_1 > 0$ so that ϕ_1 asymptotically becomes nonnegative. Therefore, it is sufficient to consider the case $0 \le \phi_1 \le \frac{\pi}{2}$. In this case, it holds $\cos(\phi_1 - \alpha_{j1}) > 0$, since $-\frac{\pi}{2} < \phi_1 - \alpha_{j1} < \frac{\pi}{2}$. Thus, we have $\dot{V}_1 < 0$ $(\forall\Phi_1 \neq 0)$, and this implies that $\Phi_1 = \dot{\phi}_1 \to 0$ from Lyapunov's stability theorem. Therefore, it is seen from (30) that

$$\phi_1 \to \sin^{-1}\frac{L}{2R_{j1}} + \alpha_{j1} \ (t \to \infty). \tag{32}$$

In the same way, it can be derived for $\phi_i (i = 2, 3)$ that

$$\phi_2 \to 2\sin^{-1}\frac{L}{2R_{j1}}, \quad \phi_3 \to 2\sin^{-1}\frac{L}{2R_{j1}}. \tag{33}$$

See Appendix B for the details on the convergence of ϕ_2 and ϕ_3.

The asymptotic value of ϕ_i, which results from (32)–(33), is illustrated in Fig. 19. Since the orientation ψ_p of unit 1 is always equivalent to the tangent direction of the path of P, it holds $\angle O_r PA = \frac{\pi}{2}$. This implies from (29) that $\angle O_r AP = \frac{\pi}{2} - \alpha_{j1}$. Therefore, $\angle O_r AB = \frac{\pi}{2} - \phi_1 + \alpha_{j1}$. Let M_2 denote the foot of the perpendicular from O_r to $\overline{AB}$, then $\angle AO_r M_2 = \phi_1 - \alpha_{j1}$. Now, since we have $\overline{AM_2} = R_{j1}\sin(\phi_1 - \alpha_{j1}) = L/2$ from (32), M_2 is also the midpoint of $\overline{AB}$ as well as the foot of the perpendicular, which implies that $\triangle O_r AM_2 \equiv \triangle O_r BM_2$. Thus, since $\triangle O_r AB$ is an isosceles triangle with $\overline{O_r A} = \overline{O_r B}$, the first and second joints are on the same circular path of radius R_{j1}. In addition, it holds from $\angle O_r AB = \angle O_r BA = \pi/2 - \phi_1 + \alpha_{j1}$ that $\angle O_r BC = \pi/2 - \phi_2 + \phi_1 - \alpha_{j1}$, which

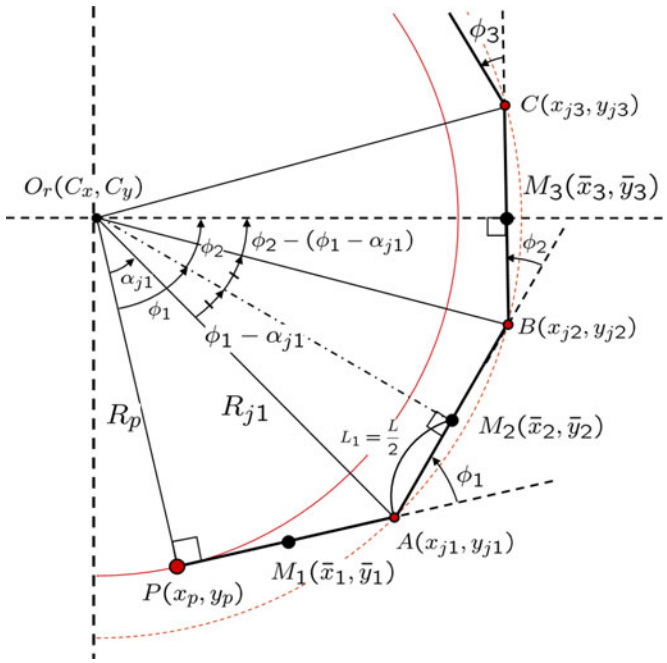

Fig. 19. Configuration asymptotically achieved for constant curvature.

implies that $\angle BO_r M_3 = \phi_2 - \phi_1 + \alpha_{j1}$ for the foot of the perpendicular M_3 from O_r to $\overline{BC}$. From (32)–(33), it holds

$$\begin{aligned} \overline{BM}_3 &= R_{j1}\sin(\phi_2 - (\phi_1 - \alpha_{j1})) \\ &= R_{j1}\sin\left(2\sin^{-1}\left(\frac{L}{2R_{j1}}\right) - \sin^{-1}\left(\frac{L}{2R_{j1}}\right)\right) = \frac{L}{2} \end{aligned} \tag{34}$$

which implies that M_3 is the midpoint of $\overline{BC}$. Thus, joint 3 is on the same circle as joints 1 and 2, since $\triangle O_r BC$ is an isosceles triangle with $\overline{O_r B} = \overline{O_r C}$. Furthermore, it is trivial to show that joint 4 at the tail is also on the same circle, since $\phi_2 = \phi_3$ from (33).

Note that it is difficult to guarantee the convergence to the target paths except for circular paths. However, the control law is expected to work well, if the curvature of the path does not changes rapidly and if there is no initial tracking error. This is because the angular velocity of each joint angle is determined under the assumptions that 1) all the joints are currently on the target path and 2) the transition rate of curvature of the target path is sufficiently small between two consecutive joints, as mentioned in Section V-B. Sections V-D and E show examples in which the control method works well for noncircular paths.

It is also important to note that the difficulty to guarantee the convergence of tracking error arises because the target path is not available in our control problem. If the target path is available, it should be easier to derive a control law using the target path information such that the convergence is guaranteed for more general target paths. However, since a human operator typically gives velocity commands in real time to the front unit in our target applications, the target path needs to be estimated based on the memory of the past commands, which is difficult in many cases due to the computational burden. Thus, the proposed

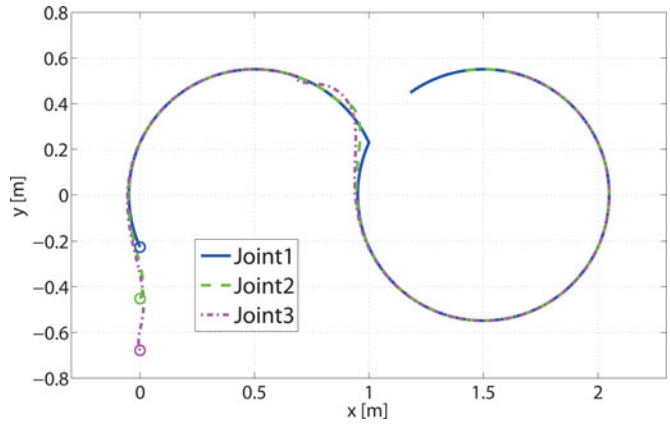

Fig. 20. x–y plot of each joint path in simulation (feedforward).

control method is not based on the past commands but only on the current velocity command.

D. Numerical Examples

The proposed method is tested for two types of target paths. The first example adopts the connected arcs as the target path. The arcs are chosen to verify the convergence of tracking error, which is theoretically shown in Section V-C. On the other hand, the second example adopts the target path whose curvature continuously changes, rather than a circular target path. Although the convergence of the tracking error is not theoretically guaranteed for such target paths, the control law is expected to work well, if the curvature of the path does not changes rapidly and if there is no initial tracking error, as mentioned at the end of Section V-C. The target path in the second example is adopted to show the effectiveness of the control method for the target paths except for circular arcs. It is also important to note that information on the target paths is not used for control in both simulations in this section and experiments in the next section. Only the velocity commands (v_1, ω_1) at the current time and joint angles $\phi_i (i = 1, 2, 3)$ are used in simulations to apply the proposed control law. The measured values of (x_p, y_p, ψ_p) at the current time are additionally used for experiments in the next section.

The command for the translational velocity v_1 of the front unit is given as $v_1 = \frac{\pi}{60}$ m/s. The angular velocity is given as $\omega_1 = -\frac{\pi}{30}$ rad/s for $t < 30$ s, and then it is switched to $\omega_1 = \frac{\pi}{30}$ rad/s for $t \geq 30$ s. This implies that the path of P is composed of two connected arcs of radius 0.5 m. As mentioned in Section V-C, the target path γ which is the path of joint 1 is an arc of radius $\sqrt{R_p^2 + L^2}$, when the path of P is an arc of radius R_p. Fig. 20 shows the paths of the joints for $0 \leq t \leq 85$ s, where the initial state is $\xi(0) = [0, 0, \frac{3}{2}\pi, 0, 0, 0]^T$. The solid, dashed, and dash–dotted lines show the paths of joints 1, 2, and 3, respectively, and "$\circ$" denotes the initial position of each joint. Although joints 2 and 3 initially deviate from the path of joint 1 due to the straight-line configuration, the tracking errors converge to 0 before $t = 30$ s when ω_1 is switched. In addition, although joints 2 and 3 are off the target path at $t = 30$ s due to the jump of the curvature of the target path around (1,0.25), the tracking errors converge to 0 without feedback control, once the curvature of the target path becomes constant, as mentioned in Section V-C.

TABLE I
TRACKING ERROR FOR $\omega_1 = -\frac{\pi}{30}\cos\lambda\frac{\pi}{60}t$

	$\lambda = 0.5$	$\lambda = 1$	$\lambda = 1.5$	$\lambda = 2$
(x_{j2}, y_{j2})	1.22×10^{-3}	1.98×10^{-3}	2.99×10^{-3}	4.07×10^{-3}
(x_{j3}, y_{j3})	2.35×10^{-3}	3.92×10^{-3}	5.94×10^{-3}	8.07×10^{-3}
(x_{j4}, y_{j4})	3.34×10^{-3}	5.80×10^{-3}	8.81×10^{-3}	1.20×10^{-2}

Next, we show an example where the curvature of the target path is continuously changing. The command for the translational velocity v_1 for the front unit is given as $v_1 = \frac{\pi}{60}$ m/s, while the angular velocity is $\omega_1 = -\frac{\pi}{30}\cos\lambda\frac{\pi}{60}t$ rad/s for a constant λ. This implies that ω_1 is changed from $-\frac{\pi}{30}$ to $\frac{\pi}{30}$ rad/s in $60/\lambda$ s. Table I shows the maximum tracking error for $\lambda = 0.5, 1, 1.5, 2$. It can be seen from Table I that, e.g., for $\lambda \leq 1$, the path-tracking error is within 5.80×10^{-3} m, i.e., 4% of the width of screw-drive units $2r = 0.15$ m. In addition, we learn from this table that the maximum error tends to increase linearly with λ. Note that although we have simply used cosine functions to change the curvature of the target path, many other types of paths, which human operators possibly give in practical situations, need to be considered in the future.

E. Experiments

In order to compare with the simulation results in Section V-D, the same velocity commands generated in advance are given for the front unit, although our experimental system is equipped with a joystick for a human operator to give velocity commands. A major difference from the numerical example is that due to the effects of modeling errors and disturbances, the feedback law as in (8) is necessary to generate a similar target path γ to the one in Section V-D. More precisely, the commands for the front unit $(\dot{x}_p, \dot{y}_p, \dot{\psi}_p)$ are given as in (8) using measurement data (x_p, y_p, ψ_p) by a vision sensor system (QuickMag IV, OKK), where

$$\dot{x}_p^d = -v_1 \cos\psi_p, \quad \dot{y}_p^d = -v_1 \sin\psi_p, \quad \dot{\psi}_p^d = \omega_1, \qquad (35)$$

and the feedback gain is chosen as $K_1 = \mathrm{diag}(1, 1, 0.5)$. Similarly to Section V-D, the command for the translational velocity v_1 for the front unit is given as $v_1 = \frac{\pi}{60}$ m/s. The angular velocity is given as $\omega_1 = -\frac{\pi}{30}$ rad/s for $t < 30$ s, and then it is switched to $\omega_1 = \frac{\pi}{30}$ rad/s for $t \geq 30$ s. Figs. 21 and 22 show the time responses of the head position and orientation, where the solid and dashed lines indicate the measurements (x_p, y_p, ψ_p) and the target trajectories (x_p^d, y_p^d, ψ_p^d), respectively. The paths of the joints for $0 \leq t \leq 85$ s in this case are shown in Fig. 23. The solid, dashed, and dash–dotted lines show the paths of joints 1, 2, and 3, respectively, and "$\circ$" denotes the initial position of each joint. It can be seen that the similar responses to the ones in Fig. 20 are obtained in Fig. 23. However, in contrast with the simulation result where there is no steady-state error, the maximum steady-state error is nearly 5 cm for the left turn. A possible reason for this is the steady-state error of (x_p, y_p, ψ_p), which is slightly larger for the left turn at $t \geq 30$, as shown

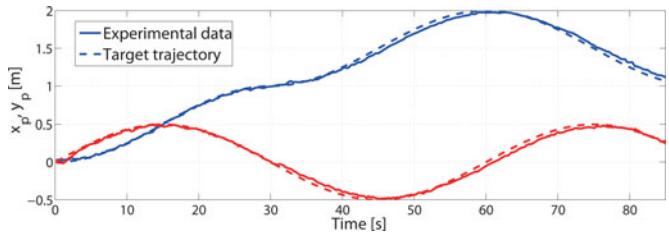

Fig. 21. Time plot of x_p and y_p in experiment (feedback).

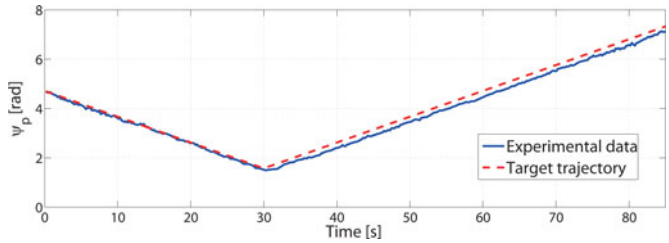

Fig. 22 Time plot of ψ_p in experiment (feedback).

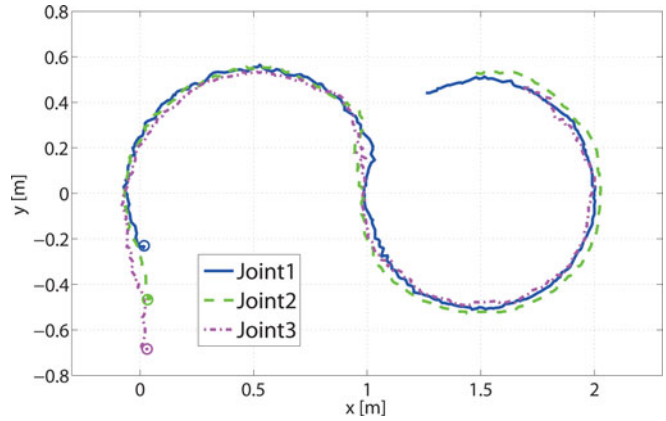

Fig. 23. x–y plot of each joint path in experiment (feedback).

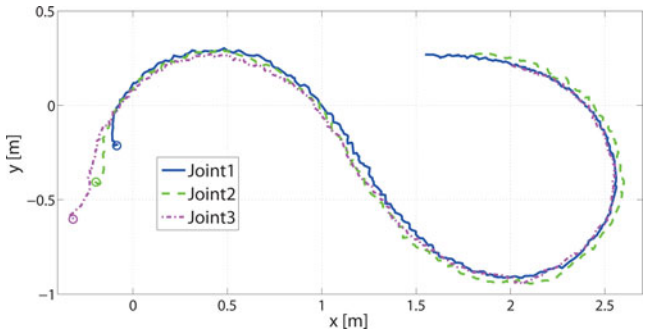

Fig. 24. x–y plot for $\omega_1 = -\frac{\pi}{30}\cos\frac{\pi}{60}t$ in experiment (feedback).

in Figs. 21 and 22. The front-unit-following controller in this paper does not take into account such steady-state error due to modeling error and disturbance. As a result, the radius of arc which joint 1 tracks is approximately 5 cm less than the target arc.

In the next example, the command for the translational velocity v_1 for the front unit is given as $v_1 = \frac{\pi}{60}$ m/s, while the angular

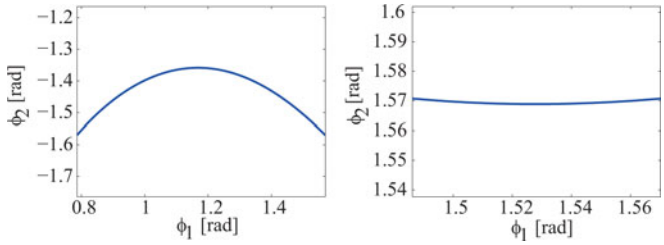

Fig. 25. (ϕ_1, ϕ_2) for which A does not have full column rank (left: $\phi_1 > 0$, $\phi_2 < 0$, right: $\phi_1 > 0$, $\phi_2 > 0$).

velocity is $\omega_1 = -\frac{\pi}{30}\cos\lambda\frac{\pi}{60}t$ rad/s for $\lambda = 1$. Fig. 24 shows paths of the joints for $0 \le t \le 95$ s, where the initial state is $\xi(0) = [0, 0, \frac{5}{3}\pi, 0, 0, 0]^T$. In contrast that the maximum tracking error is less than 4 mm in the simulation result as shown in Table I, the maximum error is about 5 cm in the experiment, similarly to the previous example in Fig. 23. Developing a control method to handle modeling errors is one of the future issues.

VI. Conclusion

In this paper, we have developed a new type of snake-like robot using screw-drive units that are connected by active joints. In addition, a kinematic model has been derived and applied to trajectory tracking control. Furthermore, we have proposed a front-unit-following controller to steer each unit to follow the path of the front unit. This controller can support manual operations, since human operators are required to command only one unit in the front. Asymptotic convergence of the tracking error of the front-unit-following controller has been analyzed based on a Lyapunov approach for the case of constant curvature. The effectiveness of the control method has been demonstrated by numerical examples and experiments. Although the kinematic model and the controllers have been presented for four link robots in accordance with the experimental system, it is possible to extend these results to more general cases of n (≥ 3) links. One of the future issues is to develop a control method to handle modeling errors due to the effects such as side slipping of the passive wheels. In addition, the tracking performance of the front-unit-following controller needs to be investigated for many types of paths, which human operators possibly give in practical situations. Furthermore, this paper has only focused on the cases where the robot does not contact with environment except for the ground, which is assumed to be flat and horizontal. The experiments have been performed only on a flat floor of indoor environments, as the first step. Many problems including the improvement of the prototype need to be tackled in order that this robot is applicable outside of laboratory environments.

Appendix A
Necessary Condition That A is not Full Column Rank

Since this paper considers the cases where $\alpha_i = -\frac{\pi}{4}$ rad$(i = 1, 3)$ and $\alpha_i = \frac{\pi}{4}$ rad$(i = 2, 4)$, we can obtain the following fact.

Proposition 1: The matrix A in (3) is not of full column rank, only if ϕ_i $(-\frac{\pi}{2} \leq \phi_i \leq \frac{\pi}{2}, i = 1, 2)$ satisfies

$$\phi_2 = \sin^{-1} \frac{D_2}{\Psi} - \beta_2 \tag{36}$$

where

$$\Psi := \sqrt{(L_1 \cos\phi_1)^2 + (L_1 \sin\phi_1 + L_2)^2}$$
$$D_2 := \frac{L}{2}(\sin 2\phi_1 - \cos 2\phi_1 - 1) - L_1 \cos\phi_1 \tag{37}$$

and β_2 is a joint angle that satisfies

$$\sin\beta_2 = \frac{L_1 \sin\phi_1 + L_2}{\Psi}, \cos\beta_2 = \frac{L_1 \cos\phi_1}{\Psi}. \tag{38}$$

Proof: From the definition of A, it is sufficient to discuss the column rank of A_{11}. Define the ith column of A_{11} as a_i, i.e., $A_{11} = [a_1, a_2, a_3]$. Then, a_1, a_2, a_3 are linearly dependent if and only if there exist scalars c_1, c_2, c_3, which are not all zero and satisfy

$$c_1 a_1 + c_2 a_2 + c_3 a_3 = 0. \tag{39}$$

From the definitions of a_1 and a_2, we have

$$a_1 = a_1' \cos\psi_p - a_2' \sin\psi_p, a_2 = a_1' \sin\psi_p + a_2' \cos\psi_p \tag{40}$$

where

$$a_1' := \begin{bmatrix} \cos\alpha_1 \\ \cos(\alpha_2 + \phi_1) \\ \cos(\alpha_3 + \phi_1 + \phi_2) \\ \cos(\alpha_4 + \phi_1 + \phi_2 + \phi_3) \end{bmatrix}$$
$$a_2' := \begin{bmatrix} \sin\alpha_1 \\ \sin(\alpha_2 + \phi_1) \\ \sin(\alpha_3 + \phi_1 + \phi_2) \\ \sin(\alpha_4 + \phi_1 + \phi_2 + \phi_3) \end{bmatrix}.$$

By substituting (40) into (39), we have

$$c_1' a_1' + c_2' a_2' + c_3 a_3 = 0 \tag{41}$$

where

$$c_1' := c_1 \cos\psi_p + c_2 \sin\psi_p, \quad c_2' := -c_1 \sin\psi_p + c_2 \cos\psi_p.$$

This implies that

$$\begin{bmatrix} c_1 \\ c_2 \end{bmatrix} = R(\psi_p) \begin{bmatrix} c_1' \\ c_2' \end{bmatrix}, \quad R(\psi_p) := \begin{bmatrix} \cos\psi_p & -\sin\psi_p \\ \sin\psi_p & \cos\psi_p \end{bmatrix}$$

where $R(\psi_p)$ is nonsingular for any ψ_p. Thus, c_1, c_2, c_3 are not all zero and satisfy (39), if and only if c_1', c_2', c_3 are not all zero and satisfy (41). Therefore, A_{11} does not have full column rank, only if ϕ_1 and ϕ_2 satisfy the equations in the first three rows of (41).

First, we consider the case of $c_3 = 0$. In this case, we can assume $c_1' = 1$ without loss of generality. By substituting $c_1' = 1$ and $\alpha_1 = -\frac{\pi}{4}$ into the first row of (41), we obtain $c_2' = -\frac{\cos\alpha_1}{\sin\alpha_1} = 1$. Thus, from the second and the third rows of (41), we have

$$\cos(\alpha_2 + \phi_1) + \sin(\alpha_2 + \phi_1) = 0$$
$$\cos(\alpha_3 + \phi_1 + \phi_2) + \sin(\alpha_3 + \phi_1 + \phi_2) = 0 \tag{42}$$

respectively. By substituting $\alpha_2 = \frac{\pi}{4}$ and $\alpha_3 = -\frac{\pi}{4}$ into (42), we have $\cos\phi_2 = 0$ and $\sin(\phi_1 + \phi_2) = 0$. This implies that $\phi_i = \frac{\pi}{2}$ or $-\frac{\pi}{2}$ $(i = 1, 2)$, which satisfies (36).

Next, we consider the case of $c_3 \neq 0$. In this case, we can assume $c_3 = 1$ without loss of generality. It follows from $\alpha_1 = -\frac{\pi}{4}$ and the first row of (41) that $c_1' = c_2' + L_1$. Thus, from the second and third rows of (41), we obtain

$$(c_2' + L_1)\cos(\alpha_2 + \phi_1) + (c_2' + L)\sin(\alpha_2 + \phi_1) + L_1 \sin\alpha_2 = 0$$
$$(c_2' + L_1)\cos(\alpha_3 + \phi_1 + \phi_2) + (c_2' + L)\sin(\alpha_3 + \phi_1 + \phi_2) + L_1 \sin\alpha_3 + L\sin(\alpha_3 + \phi_1) = 0.$$

This implies from $\alpha_2 = \frac{\pi}{4}$ and $\alpha_3 = -\frac{\pi}{4}$ that

$$(2c_2' + L_1 + L)\cos\phi_1 + (L - L_1)\sin\phi_1 + L_1 = 0 \tag{43}$$
$$(L_1 - L)\cos(\phi_1 + \phi_2) + (2c_2' + L_1 + L)\sin(\phi_1 + \phi_2) - L_1 - L\cos\phi_1 + L\sin\phi_1 = 0. \tag{44}$$

By substituting

$$2c_2' + L_1 + L = -\frac{L_1 + (L - L_1)\sin\phi_1}{\cos\phi_1} \tag{45}$$

which is obtained from (43) into (44), we have

$$(L_1 - L)\cos\phi_2 - L_1 \sin(\phi_1 + \phi_2) - L_1 \cos\phi_1 - L\cos^2\phi_1 + L\sin\phi_1\cos\phi_1 = 0. \tag{46}$$

Since (46) is written as an affine equation of $\sin\phi_2$ and $\cos\phi_2$:

$$L_1 \cos\phi_1 \sin\phi_2 + (L_1 \sin\phi_1 + L - L_1)\cos\phi_2 = \frac{L}{2}(\sin 2\phi_1 - \cos 2\phi_1 - 1) - L_1 \cos\phi_1 \tag{47}$$

ϕ_2 can be described as (36). ■

As shown in the proof, A is not of full column rank for $\phi_i = \frac{\pi}{2}$ or $-\frac{\pi}{2}$ $(i = 1, 2)$. Fig. 25 shows other sets of (ϕ_1, ϕ_2) which satisfy (36). The figure on the left shows the case where $\phi_1 > 0$ and $\phi_2 < 0$, while the case where $\phi_1 > 0$ and $\phi_2 > 0$ is shown on the right. Note that there is no set of (ϕ_1, ϕ_2), which satisfies (36), in the case of $-\frac{\pi}{2} < \phi_1, \phi_2 < 0$ and the case of $-\frac{\pi}{2} < \phi_1 < 0$ and $0 < \phi_2 < \frac{\pi}{2}$.

As shown in Fig. 25 (left), in the case of $\phi_1 > 0$ and $\phi_2 < 0$, the robot has a zig–zag shape with $\phi_1 - \phi_2 > 2.35$ rad and $\phi_2 < -1.35$ rad. Fig. 25 (right) shows that (36) is satisfied only for $\phi_1 \simeq \phi_2 \simeq \frac{\pi}{2}$ in the case where $\phi_1 > 0$ and $\phi_2 > 0$.

APPENDIX B
CONVERGENCE OF JOINT ANGLES ϕ_2 AND ϕ_3

As shown in Section V-C, the angle of joint 1 converges to a constant value in (32). Therefore, we investigate the

convergence properties of ϕ_2 and ϕ_3 for

$$\phi_1 = \sin^{-1}\frac{L}{2R_{j1}} + \alpha_{j1}, \quad \dot{\phi}_1 = 0. \tag{48}$$

From (17) and (48), it holds that

$$\begin{aligned}\Phi_2 &:= \dot{\phi}_2 = \dot{\psi}_3 - \dot{\psi}_p - \dot{\phi}_1 \\ &= \frac{2}{L}\{\dot{x}_{j2}\sin\psi_3 - \dot{y}_{j2}\cos\psi_3\} - \omega_1. \end{aligned}\tag{49}$$

Since (11) and the derivative of (28) imply that

$$\begin{aligned}&\dot{x}_{j2}\sin\psi_3 - \dot{y}_{j2}\cos\psi_3 = \dot{x}_{j1}\sin\psi_3 - \dot{y}_{j1}\cos\psi_3 \\ &- L\dot{\psi}_2(\sin\psi_2\sin\psi_3 + \cos\psi_2\cos\psi_3) \\ &= R_{j1}\omega_1\sin(\psi_3 - (\psi_p + \alpha_{j1})) - L\omega_1\cos\phi_2\end{aligned}$$

we have

$$\Phi_2 = \frac{2\omega_1}{L}\{R_{j1}\sin(\phi_1 + \phi_2 - \alpha_{j1}) - L\cos\phi_2\} - \omega_1. \tag{50}$$

Furthermore, by substituting ϕ_1 in (48) into (50), it holds

$$\begin{aligned}\Phi_2 &= \frac{2\omega_1}{L}\left\{R_{j1}\sin(\sin^{-1}\frac{L}{2R_{j1}} + \phi_2) - L\cos\phi_2\right\} - \omega_1 \\ &= \frac{2\omega_1}{L}\left\{R_{j1}\cos(\sin^{-1}\frac{L}{2R_{j1}})\sin\phi_2 - \frac{L}{2}\cos\phi_2\right\} - \omega_1 \\ &= \frac{2\omega_1}{L}\left\{\sqrt{R_{j1}^2 - \frac{L^2}{4}}\sin\phi_2 - \frac{L}{2}\cos\phi_2\right\} - \omega_1 \\ &= \frac{2\omega_1}{L}R_{j1}\sin(\phi_2 + \alpha_{j2}) - \omega_1\end{aligned}\tag{51}$$

where

$$\alpha_{j2} = \cos^{-1}\tfrac{1}{R_{j1}}\sqrt{R_{j1}^2 - (\tfrac{L}{2})^2} = -\sin^{-1}\tfrac{L}{2R_{j1}}. \tag{52}$$

Thus, from $R_{j1} > L > 0$, we assume that $-\frac{\pi}{2} < \alpha_{j2} < 0$ without loss of generality. Then, for $V_2 := \frac{1}{2}\Phi_2^2$, it holds

$$\dot{V}_2 = \Phi_2\dot{\Phi}_2 = \Phi_2^2\frac{2R_{j1}\omega_1}{L}\cos(\phi_2 + \alpha_{j2}). \tag{53}$$

Using a similar procedure to the one for (31), it holds

$$\Phi_2 = \frac{2\omega_1}{L}R_{j1}\sin(\phi_2 + \alpha_{j2}) - \omega_1 \to 0 \tag{54}$$

since we have a constraint as $-\frac{\pi}{2} \le \phi_2 \le \frac{\pi}{2}$. Therefore, it holds from (54) that

$$\phi_2 \to \sin^{-1}\frac{L}{2R_{j1}} - \alpha_{j2} = 2\sin^{-1}\frac{L}{2R_{j1}}. \tag{55}$$

Now we investigate the convergence property of ϕ_3 for $\phi_2 = 2\sin^{-1}\frac{L}{2R_{j1}}$ and $\dot{\phi}_2 = 0$. Similarly to (49)–(51), it holds that

$$\begin{aligned}\Phi_3 &:= \dot{\phi}_3 = \dot{\psi}_4 - \dot{\psi}_p - \dot{\phi}_1 - \dot{\phi}_2 \\ &= \frac{2\omega_1}{L}R_{j1}\sin(\phi_3 + \alpha_{j2}) - \omega_1.\end{aligned}\tag{56}$$

Since (51) and (56) have the same form, it holds that $\phi_3 \to 2\sin^{-1}\frac{L}{2R_{j1}}$, similarly to (55).

ACKNOWLEDGMENT

The authors would like to thank H. Igarashi and M. Hara for assistance to set up the experimental system in this paper.

REFERENCES

[1] T. Kamegawa, T. Yamasaki, H. Igarashi, and F. Matsuno, "Development of the snake-like rescue robot KOHGA," in *Proc. IEEE Int. Conf. Robot. Autom.*, 2004, pp. 5081–5086.
[2] T. Takayama and S. Hirose, "Development of "Souryu I & II"—Connected crawler vehicle for inspection of narrow and winding space," *J. Robot. Mech.*, vol. 15, no. 1, pp. 61–69, 2001.
[3] K. Suzumori, S. Wakimoto, and M. Takata, "A miniature inspection robot negotiating pipes of widely varying diameter," in *Proc. IEEE Int. Conf. Robot. Autom.*, 2003, pp. 2736–2740.
[4] A. Kuwada, S. Wakimoto, K. Suzumori, and Y. Adomi, "Automatic pipe negotiation control for snake-like robot," in *Proc. IEEE/ASME Int. Conf. Adv. Intell. Mechatron.*, 2008, pp. 558–563.
[5] S. Hirose, *Biologically Inspired Robots: Snake-Like Locomotors and Manipulators*. Oxford, U.K.: Oxford Univ. Press, 1993.
[6] J. Ostrowski and J. Burdick, "Gait kinematics for a serpentine robot," in *Proc. IEEE Int. Conf. Robot. Autom.*, 1996, pp. 1294–1299.
[7] P. Prautsch and T. Mita, "Control and analysis of the gait of snake robots," in *Proc. IEEE Int. Conf. Control Appl.*, 1999, pp. 502–507.
[8] F. Matsuno and K. Mogi, "Redundancy controllable system and control of snake robots based on kinematic model," in *Proc. IEEE Conf. Decis. Control*, 2000, pp. 4791–4796.
[9] S. Ma, "Analysis of creeping locomotion of a snake-like robot," *Adv. Robot.*, vol. 15, no. 2, pp. 205–224, 2001.
[10] M. Saito, M. Fukaya, and T. Iwasaki, "Serpentine locomotion with robotic snakes," *IEEE Control Syst. Mag.*, vol. 22, no. 1, pp. 64–81, Feb. 2002.
[11] T. Kamegawa and F. Matsuno, "Proposition of twisting mode of locomotion and GA based motion planning for transition of locomotion modes of 3-dimensional snake-like robot," in *Proc. IEEE Int. Conf. Robot. Autom.*, 2002, pp. 1507–1512.
[12] A. A. Transeth, R. I. Leine, C. Glocker, K. Y. Pettersen, and P. Liljebäck, "Snake robot obstacle-aided locomotion: modeling, simulations, and experiments," *IEEE Trans. Robot.*, vol. 24, no. 1, pp. 88–104, Feb. 2008.
[13] R. L. Hatton and H. Choset, "Generating gaits for snake robots: Annealed chain fitting and keyframe wave extraction," *Auton. Robot.*, vol. 28, pp. 271–281, 2010.
[14] X. Wu and S. Ma, "Adaptive creeping locomotion of a CPG-controlled snake-like robot to environment change," *Auton. Robot.*, vol. 28, pp. 283–294, 2010.
[15] P. Liljebäck, K. Y. Pettersen, Ø. Stavdahl, and J. T. Gravdahl, "Controllability and stability analysis of planar snake robot locomotion," *IEEE Trans. Automat. Contr.*, vol. 56, no. 6, pp. 1365–1380, Jun. 2011.
[16] K. Osuka and H. Kitajima, "Development of mobile inspection robot for rescue activities: MOIRA," in *Proc. IEEE/RSJ Int. Conf. Intell. Robots Syst.*, 2003, pp. 3373–3377.
[17] J. Borenstein, M. Hansen, and A. Borrell, "The OmniTread OT-4 serpentine robot—Design and performance," *J. Field Robot.*, vol. 24, no. 7, pp. 601–621, 2007.
[18] S. Hirose, H. Ohno, T. Mitsui, and K. Suyama, "Design and experiments of in-pipe inspection vehicles for $\phi 25, \phi 50, \phi 250$ pipes," *J. Robot. Mech.*, vol. 12, no. 3, pp. 310–317, 2000.
[19] T. Yamaguchi, Y. Kagawa, I. Hayashi, N. Iwatsuki, K. Morikawa, and K. Nakamura, "Screw principle microrobot passing steps in a small pipe," in *Proc. Int. Symp. Micromechatron. Human Sci.*, 1999, pp. 149–152.
[20] A. Kakogawa and S. Ma, "Mobility of an in-pipe robot with screw drive mechanism inside curved pipes," in *Proc. IEEE Int. Conf. Robot. Biomimet.*, 2010, pp. 1530–1535.
[21] F. Matsuno and T. Kawai, "Propulsion system based on screw drive mechanism," Japanese published Patent Application 2003–293656, 2003.
[22] M. Sampei, T. Tamura, T. Kobayashi, and N. Shibui, "Arbitrary path tracking control of articulated vehicles using nonlinear control theory," *IEEE Trans. Control Syst. Technol.*, vol. 3, no. 1, pp. 125–131, Mar. 1995.

[23] C. Altafini, "A Path-tracking criterion for an LHD articulated vehicle," *Int. J. Robot. Res.*, vol. 18, pp. 435–441, 1999.
[24] C. Altafini, "Path following with reduced off-tracking for multibody wheeled vehicles," *IEEE Trans. Cont. Sys. Tech.*, vol. 11, no. 4, pp. 598–605, Jul. 2003.

Hiroaki Fukushima (M'06) received the B.S. and M.S. degrees in engineering and the Ph.D. degree in informatics from Kyoto University, Kyoto, Japan, in 1995, 1998, and 2001, respectively.

From 1999 to 2004, he was a Research Fellow of the Japan Society for the Promotion of Science. From 2001 to 2003, he was a Visiting Scholar with the University of California at San Diego. From 2004 to 2009, he was a Research Associate and Assistant Professor at the University of Electro-Communications, Tokyo, Japan. He is currently an Assistant Professor with Kyoto University. His research interests include system identification and robust control.

Dr. Fukushima received the Institute of Systems, Control, and Information Engineer (ISCIE) Young Author Award in 2001 and the Society for Instrument and Control Engineers (SICE) paper award in 2003. He is a member of the SICE, ISCIE, and Robotics Society of Japan.

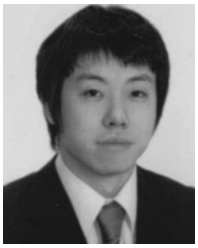

Shogo Satomura received the B.S. and M.S. degrees in engineering from the University of Electro-Communications, Tokyo, Japan, in 2004 and 2006, respectively. His master's degree focused on rescue robot systems and snake-like robots.

He is currently working with Canon, Inc., Tokyo, Japan.

Toru Kawai received the B.S. degree from the Tokyo University of Agriculture and Technology, Tokyo, Japan, and the M.S. degree from the Tokyo Institute of Technology, Tokyo, in 2001 and 2003, respectively, both in engineering. His master's degree focused on rescue robot systems and snake-like robots.

From 2003 to 2006, he was with Mitsubishi Heavy Industries, Ltd., Tokyo. He is currently with Honda R&D, Co., Ltd., Saitama, Japan.

Motoyasu Tanaka received the B.S., M.S., and Ph.D. degrees in engineering from the University of Electro-Communications, Tokyo, Japan, in 2005, 2007, and 2009, respectively.

He is currently with Canon, Inc., Saitama, Japan. His research interests include robotics and control, especially snake-like robots.

Dr. Tanaka received the Hatakeyama Memorial Prize and the Miura Memorial Prize from the Japan Society of Mechanical Engineers in 2004 and 2006, respectively, and the IEEE Robotics and Automation Society Japan Chapter Young Award from the IEEE Robotics and Automation Society Japan Chapter in 2006. He is a member of the Robotics Society of Japan.

Tetsushi Kamegawa received the B.S., M.S., and Ph.D. degrees in engineering from the Tokyo Institute of Technology, Tokyo, Japan, in 1999, 2001 and 2004, respectively.

In 2004, he was a Visiting Scholar with Roma University, Rome, Italy. From 2004 to 2006, he was a Researcher with International Rescue System Institute, Kobe, Japan. From 2006 to 2008, he was a Research Associate and Assistant Professor at Okayama University, Japan. He is currently a Senior Assistant Professor with Okayama University.

Dr. Kamegawa received the Society of Instrument and Control Engineers (SICE) Interactive Organized Session Paper Awards in 2008. He is a member of the Japan Society of Mechanical Engineers, Robotics Society of Japan, SICE, and Institute of Systems, Control, and Information Engineers.

Fumitoshi Matsuno (M'94) received the Ph.D. (Dr. Eng.) degree from Osaka University, Osaka, Japan, in 1986.

In 1986, he joined the Department of Control Engineering, Osaka University. He became a Lecturer and Associate Professor in 1991 and 1992, respectively, in the Department of Systems Engineering, Kobe University. In 1996, he joined the Department of Computational Intelligence and Systems Science, Interdisciplinary Graduate School of Science and Engineering, Tokyo Institute of Technology, as an Associate Professor. In 2003, he became a Professor with the Department of Mechanical Engineering and Intelligent Systems, University of Electro-Communications. Since 2009, he has been a Professor with the Department of Mechanical Engineering and Science, Kyoto University, Kyoto, Japan. He is also the Vice-President of NPO International Rescue System Institute (IRS). His current research interests include robotics, control of distributed parameter system and nonlinear system, rescue support system in fire and disaster, and geographic information system.

Dr. Matsuno received many awards including the Outstanding Paper Award in 2001 and 2006, the Takeda Memorial Prize in 2001 from the Society of Instrument and Control Engineers. He is a member of the Society of Instrument and Control Engineers (SICE), the Japan Society of Mechanical Engineers, the Robotics Society of Japan, and the Institute of Systems, Control and Information Engineers, among other organizations. He is a Co-chair of the IEEE Robotics and Automation Society Technical Committee on safety, security, and rescue robotics; a Chair of Steering Committee of SICE Annual Conference; an Editor of the *Journal of Intelligent and Robotic Systems*, an Associate Editor of *Advanced Robotics*, *International Journal of Control, Automation, and Systems*, etc., and on the Conference Editorial Board of the IEEE Control Systems Society.